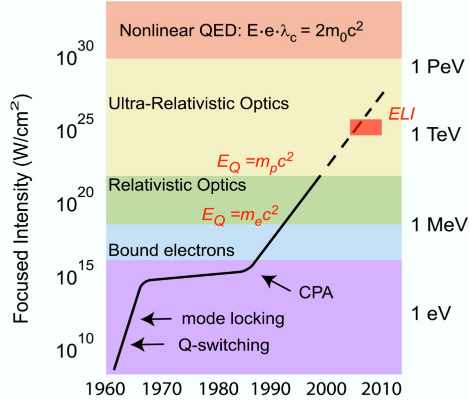

Figure taken from ELI proposal

ELI: Extreme Light Infrastructure

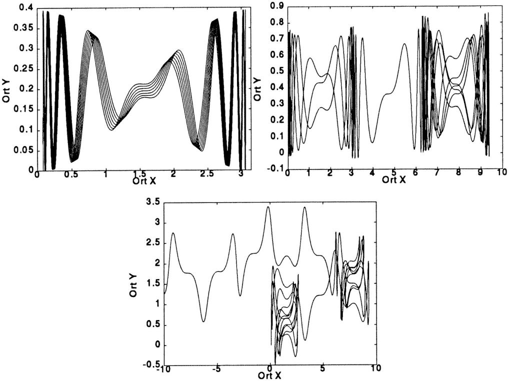

Figure 2.1: Trajectories of an electron in a standing laser wave (2.15) (polarized along $\boldsymbol{e}_y$, propagation directions along $\boldsymbol{e}_x$) that starts at $t = 0$ from $y = 0$ and $kx = \pi/40$. The amplitudes were $e\hat{A}/mc = -e\hat{E}/m\omega c = -0.1$ (upper left), -0.2 (upper right), and -0.5 (lower). With increasing laser intensity, the electron is able to escape from the "valley" in which it is released. It can then be trapped temporarily in other valleys (upper right and lower plot), and the dynamics can be shown to become chaotic.

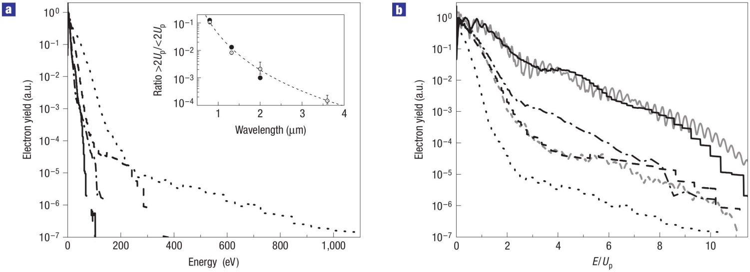

Figure 1 Comparison of photoelectron distributions of argon for different excitations at constant intensity. Excitation is at 0.8 μm (solid line), 1.3 μm (dot–dashed line), 2 μm (dashed line) and 3.6 μm (dotted line) and intensity is 0.08 PW cm^{-2}. **a**,**b**, The plots are shown in absolute (**a**) and scaled (**b**) energy (normalized against the wavelength-dependent ponderomotive energy). For this intensity U_p is approximately 5 eV, 13 eV, 30 eV and 100 eV for wavelengths of 0.8 μm, 1.3 μm, 2 μm and 3.6 μm, respectively. Also shown in **b** are the TDSE calculations (grey lines) at 0.8 μm (solid line) and 2 μm (dashed line), simulating the experimental conditions (see the Methods section). The agreement between experiment and theory is very good and reproduces the loss of resonant structure at the longer wavelength. The inset in **a** is a plot of the electron yield ratio ($>2U_p/<2U_p$) determined by the experiment (open circle, with error bars) and the TDSE calculations (closed circle) as a function of wavelength. The dashed line illustrates a $\lambda^{-4.4}$ dependence. The 1.3 μm distribution calculated using TDSE is omitted for clarity of presentation but yields similar agreement with the experiment. The resulting 1.3 μm ratio derived from the calculation is plotted in the inset. The error bars reflect the uncertainty in the intensity used in the evaluation of U_p.

Colosimo *et al.*, Nature Physics **4**, 386 (2008)

Numerical “stereo ATI” spectra

H(1s), $E(t) = \hat{E}\sin^2(\omega t/(2N))\cos(\omega t + \varphi)$, $N = 4$, $\lambda = 800\,\mathrm{nm}$, $I = 2.4 \cdot 10^{14}\,\mathrm{W/cm^2}$

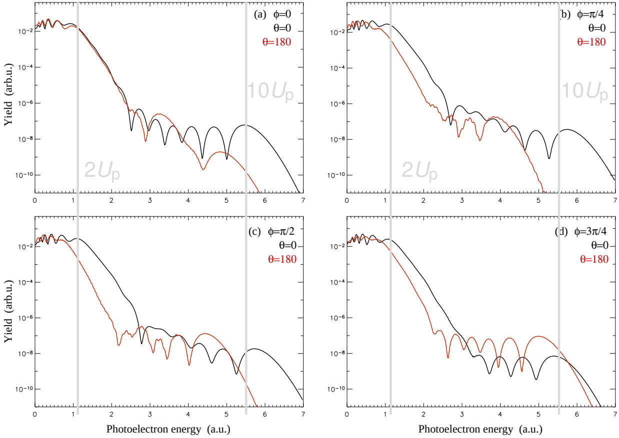

$$U_p = \frac{\hat{E}^2}{4\omega^2}$$

Numerical “stereo ATI” spectra

H(1s), $E(t) = \hat{E} \sin^2(\omega t/(2N)) \cos(\omega t + \varphi)$, $N = 4$, $\lambda = 800\,\text{nm}$, $I = 2.4 \cdot 10^{14}\,\text{W/cm}^2$

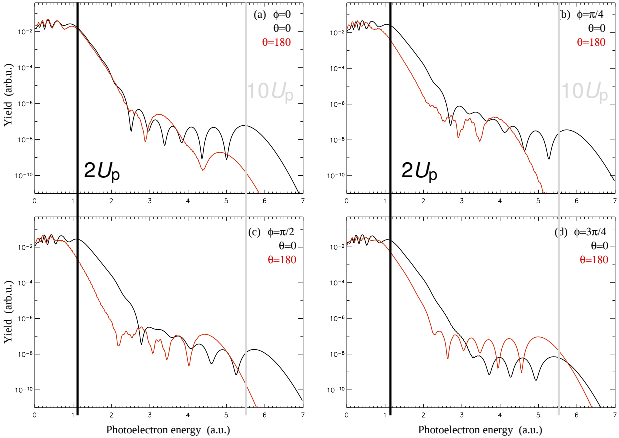

$$U_\text{p} = \frac{\hat{E}^2}{4\omega^2}$$

Numerical “stereo ATI” spectra

H(1s), $E(t) = \hat{E}\sin^2(\omega t/(2N))\cos(\omega t + \varphi)$, $N = 4$, $\lambda = 800\,\text{nm}$, $I = 2.4 \cdot 10^{14}\,\text{W/cm}^2$

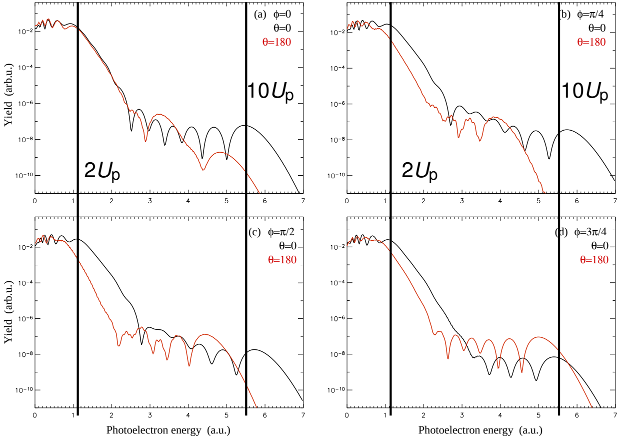

$$U_p = \frac{\hat{E}^2}{4\omega^2}$$

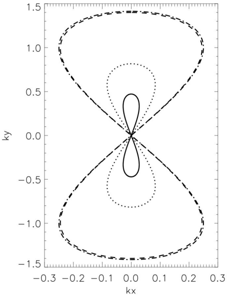

Figure 2.2: Figure-eight dynamics of a charged particle in an electromagnetic wave, as seen in the oscillation center frame. The trajectory in the xy-plane, where x is the propagation direction of the laser pulse, and y is the polarization direction, is shown for $a = 0.5$ (solid), $a = 1$ (dotted), $a = 10$ (dashed), and $a = 100$ (dashed-dotted). As a increases, the amplitudes $k\hat{x}$ and $k\hat{y}$ approach the calculated values $1/4$ and $\sqrt{2}$, respectively.

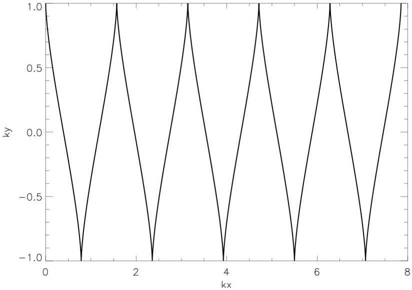

Figure 2.3: Particle motion in the lab frame for $a = 1$. While oscillating in polarization direction, the particle is drifting in propagation direction. The laser pulse is adiabatically ramped up and of constant amplitude afterwards. The particle was initially at rest. Note that there is no backward motion in x-direction (no loops but spikes).

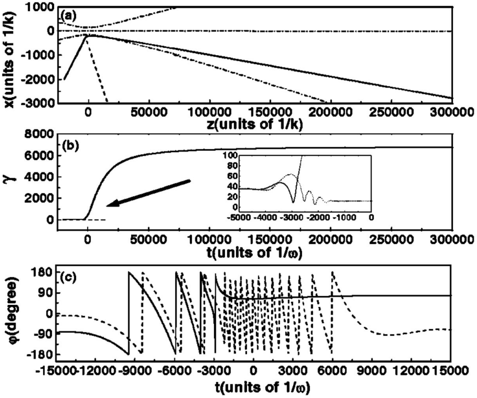

FIG. 1. Two typical cases of electron dynamics. Capture and acceleration scenario (CAS) is given by the solid line and inelastic scattering (IS) is given by the dotted line. A continuous laser beam with field intensity $a_0 = 100$ is used. Other parameters are $kw_0 = 150$, $kZ_R = 11{,}250$, $P_{xi} = 3.5$, $P_{yi} = 0$, and $P_{zi} = 35$. In the electron capture case, we terminate the calculation at $\omega t = 3 \times 10^5$. (a) Electron trajectories in the $x-z$ plane. The dot-dashed lines show the space profile of focused laser beam. (b) Electron energy γ as a function of time. The inset is the enlargement of the region denoted by the arrow shown in (b). (c) The laser wave phase experienced by the electron as a function of time.

P.X. Wang *et al.*, Appl. Phys. Lett. **78**, 2253 (2001)

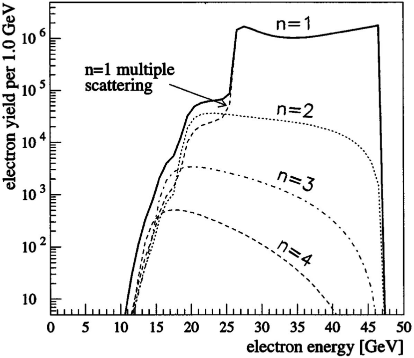

FIG. 1. Calculated yield of scattered electrons from the collision of 5×10^9 46.6-GeV electrons with a circularly polarized 1054-nm laser pulse of intensity parameter $\eta = 0.5$.

C. Bula *et al.*, Phys. Rev. Lett. **76**, 3116 (1996)

lin. Compton-Streuung: $\mathcal{E}' \in [25.6, 46.6]$ GeV, kleinere Energien entweder wegen Mehrfach- oder Multiphotonen-Compton-Streuung

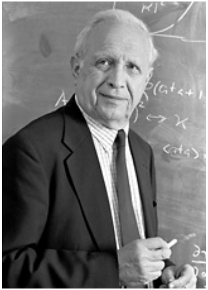

Roy J. Glauber, Nobelpreis Physik 2005

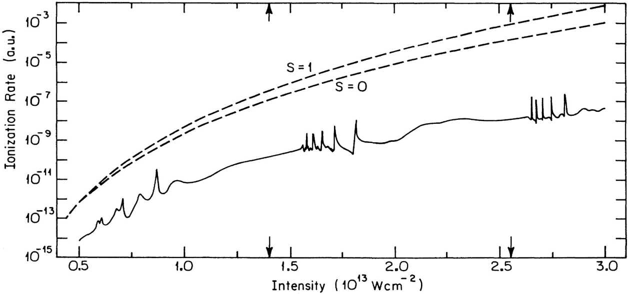

FIG. 4. Total ionization rate vs intensity for H(1*s*) irradiated by linearly polarized light of wavelength 1064 nm. Dashed curves are partial rates for $(12+S)$-photon ionization obtained within lowest-order perturbation theory. The arrows indicate the intensities at which the real part of the 1*s* Floquet eigenvalue crosses the 13- and 14-photon ionization thresholds.

R.M. Potvliege, R. Shakeshaft, Phys. Rev. A **40**, 3061 (1989)

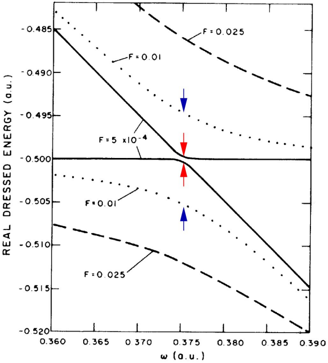

Figure 3.12: Real part of the quasi-energy ϵ for laser-driven atomic hydrogen as a function of the laser frequency ω and for three different driver amplitudes $\hat{E} = F$, as given in the plot. Avoided crossings occur at the 1s ↔ 2p-resonance frequency $\omega = 0.375$. The separations of the quasi-energies at resonance (indicated by the colored arrows) equal the corresponding Rabi-frequencies. [From A. MAQUET, SHIH-I CHU, and WILLIAM P. REINHARDT, *Stark ionization in dc and ac fields: An L^2 complex-coordinate approach*, Phys. Rev. A **27**, 2946 (1983)

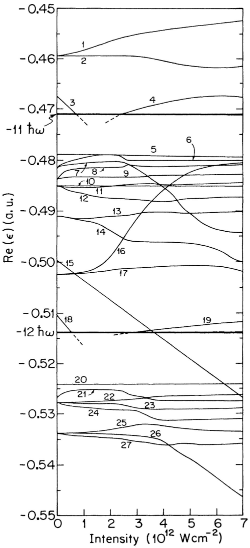

FIG. 3. Real parts of various eigenvalues ε_j for hydrogen irradiated by linearly polarized light of wavelength 1064 nm. We show $\mathrm{Re}(\varepsilon_j)-N_j\hbar\omega$, where the integer index j labels the following atomic configurations (or superpositions of configurations), where known, in the weak-intensity limit. (1–2): superpositions of 4*s* and 4*d*, $N_{1-2}=10$; (3): 2*s*, $N_3=8$; (4): unknown; (5): superposition of 8*p*, 8*f*, 8*h*, and 8*j*, $N_5=11$; (6–7): superpositions of 7*p*, 7*f*, and 7*h*, $N_{6-7}=11$; (8–9): superpositions of 3*s* and 3*d*, $N_{8-9}=10$; (10–12): superpositions of 6*p*, 6*f*, and 6*h*, $N_{10-12}=11$; (13–14): superpositions of 5*p* and 5*f*, $N_{13-14}=11$; (15): 1*s*, $N_{15}=0$; (16–17): superpositions of 4*p* and 4*f*; $N_{16-17}=11$; (18): 2*p*, $N_{18}=9$; (19): unknown; (20): superposition of 7*s*, 7*d*, 7*g*, and 7*i*, $N_{20}=12$; (21): 3*p*, $N_{21}=11$; (22–24): superpositions of 6*s*, 6*d*, and 6*g*, $N_{22-24}=12$; (25–27): superpositions of 5*s*, 5*d*, and 5*g*, $N_{25-27}=12$. We did not include states with orbital angular momentum quantum number greater than 7. The bold horizontal lines indicate multiphoton ionization thresholds. Note that reduced mass effects are included, so that, for example, $\mathrm{Re}(\varepsilon_{15})$ approaches a value slightly above -0.5 a.u. in the zero-intensity limit.

R.M. Potvliege, R. Shakeshaft, Phys. Rev. A **40**, 3061 (1989)

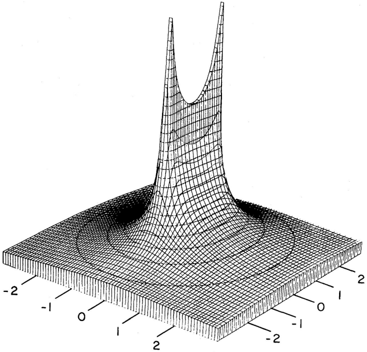

FIG. 1. Values of the dressed Coulomb potential V_0 in a plane passing through the symmetry axis defined by $\vec{\alpha}_0$. In this plane, taken as the horizontal base of the figure, distances are measured in units of α_0. Along the vertical we represent $(-\alpha_0 V_0/Z)$ in atomic units, up to the value 10. The saddle of the figure reflects the rise in V_0 near the line of singularities (extending from $-\vec{\alpha}_0$ to $\vec{\alpha}_0$) and their increasing strength towards the end points. At radial distances larger than α_0 in the horizontal plane, the distortion of the Coulomb potential fades away (the level lines become circular).

M. Gavrila and J.Z. Kamiński, Phys. Rev. Lett. **52**, 613 (1984)

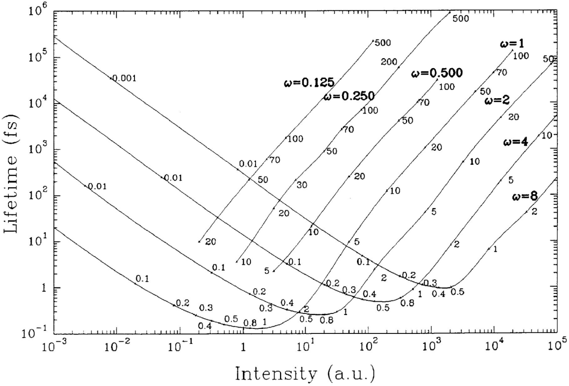

Figure 3.15: Lifetime of the H atom in the ground state according to the high-frequency Floquet theory, vs intensity, at various laser frequencies ω; circular polarization. Numbers adjacent to points on the curves are the corresponding values of $\hat{\alpha}$. The descending branches of the curves correspond to LOPT, the ascending ones to adiabatic stabilization (the latter can be “trusted” as the laser frequency increases beyond the ionization potential 0.5). [From M. PONT AND M. GAVRILA, *Stabilization of atomic hydrogen in superintense, high-frequency laser fields of circular polarization*, Phys. Rev. Lett. **65**, 2362 (1990).]

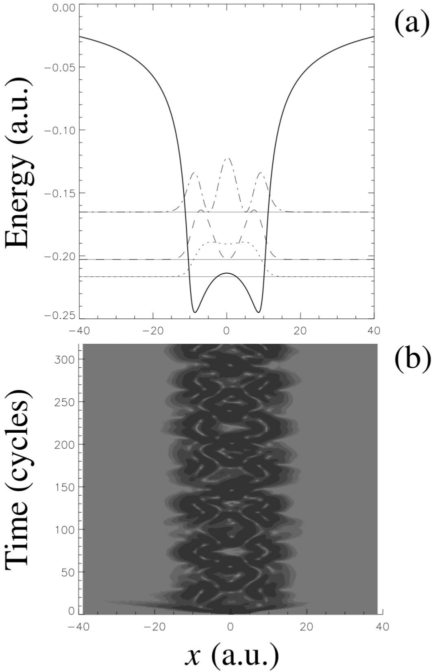
(a)
Energy (a.u.)
0.00
−0.05
−0.10
−0.15
−0.20
−0.25
−40
−20
0
20
40
(b)
Time (cycles)
300
250
200
150
100
50
0
−40
−20
0
20
40
x (a.u.)

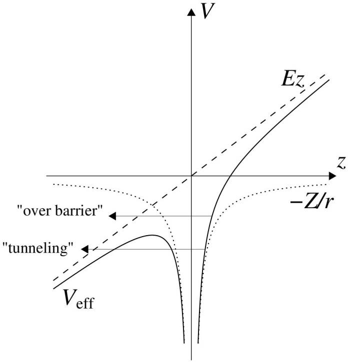

Figure 3.4: Effective potential V_{eff} in field direction. The unperturbed Coulomb potential and the field potential are also shown separately. Depending on the initial (and possibly Stark-shifted) state, the electron may either escape via tunneling or classically via “over-barrier” ionization.

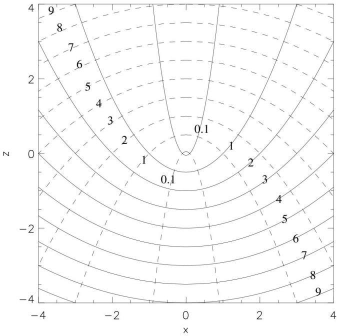

Figure 3.5: Illustration of parabolic coordinates. Cuts of contours $\xi = \mathrm{const.}$ (dashed, values given next to the lines) and $\eta = \mathrm{const.}$ (solid) in the xz-plane (azimuthal symmetry with respect to the z-axis!).

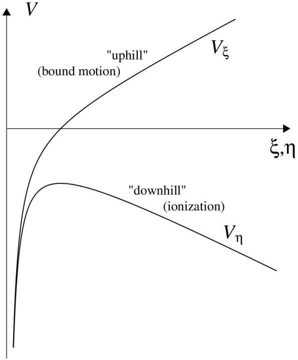

Figure 3.6: Illustration of the potentials V_ξ and V_η [Eqs. (3.201)]. The "uphill potential" V_ξ (for $E > 0$) supports only bound states while the "downhill potential" V_η displays a barrier through which the electron may tunnel.

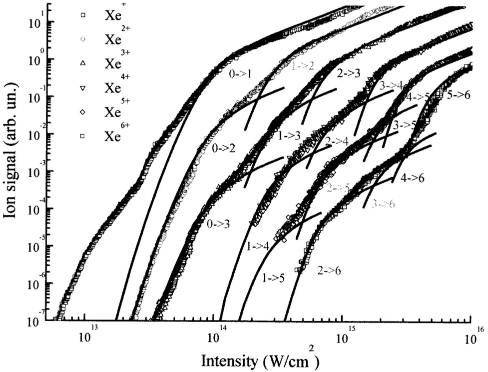

Figure 3. Multiphoton ionization of Xe using linearly polarized laser pulses from a Ti:Sapphire laser (800 nm). Each datum corresponds to a five-point average. The ion yields calculated using formula (1) are given by the curves. The numbers written on the graph indicate the transition that contributes most to a part of the curve (initial charge state→final state). For each charge state ($n < 2$), the sum of the corresponding curves follows the experimental ion yield.

S. Larochelle *et al.*, J. Phys. B **31**, 1201 (1998)

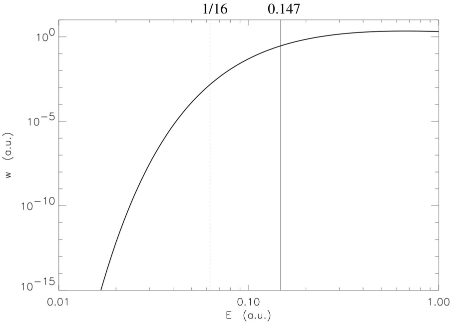

Figure 3.8: The LANDAU-rate (3.238) vs field strength E. The vertical lines indicate the (here wrong) over-barrier field strength (3.192) ($1/16$, dashed) and the correct (3.214) 0.147 (solid), respectively.

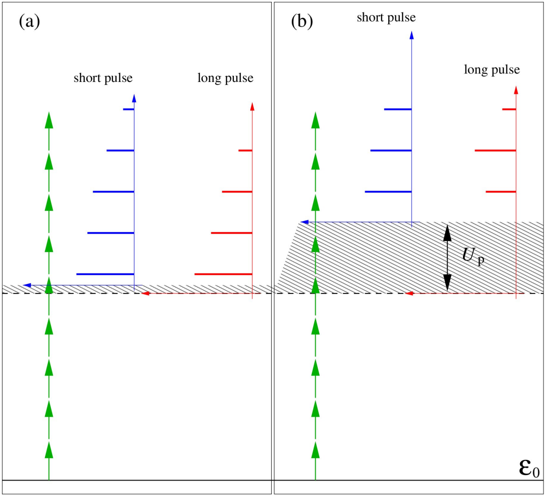

Figure 3.16: Channel closing in the short and long pulse regime. In (a) the laser intensity is small so that the U_p-shift of the continuum threshold is less than a photon energy. In (b) the channels $n = 5$ and $n = 6$ are closed due to the pronounced AC Stark shift of the continuum. The photoelectron spectra look different in the short (blue) and long pulse regime (red) since the released electron gains U_p in the latter case upon leaving the laser focus.

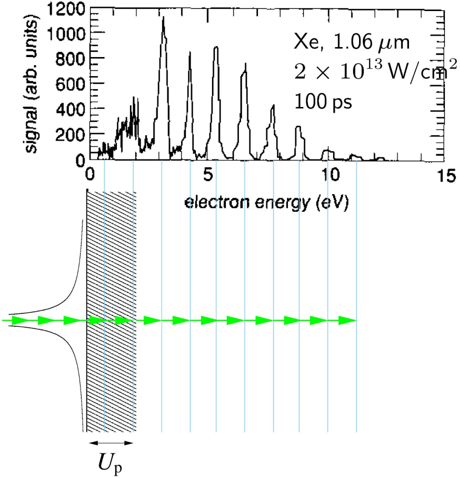

Figure 3.17: Channel closing in the long-pulse regime. The experimental spectrum was taken from R.R. FREEMAN & P.H. BUCKSBAUM, *Investigation of above-threshold ionization using sub-picosecond laser pulses*, J. Phys. B: At. Mol. Opt. Phys. **24**, 325 (1991).

Der Doppelspalt in der Zeit

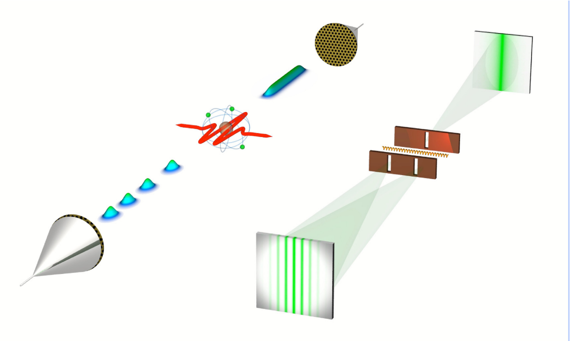

F. Lindner, M.G. Schätzel, H. Walther, A. Baltuška, E. Goulielmakis, F. Krausz, D.B. Milošević, D. Bauer, W. Becker, and G.G. Paulus,

Phys. Rev. Lett. **95**, 040401 (2005)

Lange Pulse: ein Gitter in der Zeit

Viele Zeitfenster → scharfe Peaks im Abstand von $\hbar\omega$

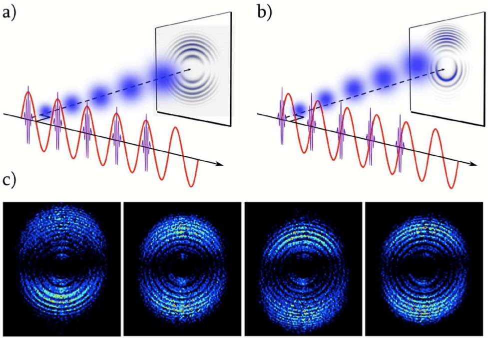

J. Mauritsson *et al.*, Phys. Rev. Lett. **100**, 073003 (2008)

“Einzyklenpulse”: Doppelspalt in der Zeit

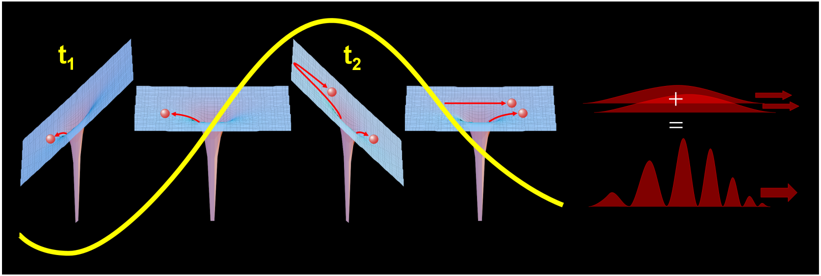

Presseerklärung, Max-Planck-Institut für Kernphysik (http://idw-online.de/pages/en/news?id=327477)

“Einzyklenpulse”: Doppelspalt in der Zeit

Zwei Zeitfenster → “keine Zeit” für scharfe Peaks

TDSE-Rechnung:

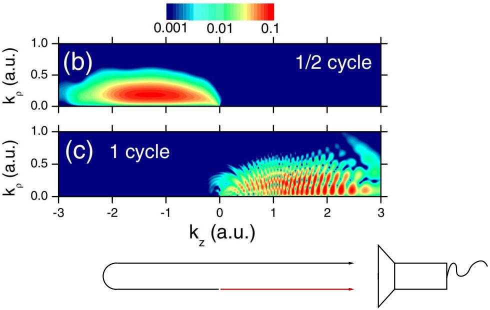

Diego G. Arbó, Emil Persson, and Joachim Burgdörfer *et al.*, Phys. Rev. A **74**, 063407 (2006)

Quantenbahnen

— Beispiel I

- 4-Zyklen-$\sin^2$-Puls, $\omega = 0.056$, $\hat{E} = -\omega\hat{A} = 0.1$, $\varphi_{\mathrm{cep}} = 0$. $A(t)$ (durchgezogen), $E(t)$ (gestrichelt).

(a) Sattelpunktzeiten t_s in der komplexen Ebene;
+/- bzgl.
$\mathbf{A}(t_s) = -p_\parallel \pm \mathrm{i}\sqrt{2I + p_\perp^2}$,
schwarz: positiver Endimpuls $p_\parallel$,
rot: negativer Endimpuls $p_\parallel$.

(b) Endimpuls $p_\parallel$ vs Ionisationszeit $\Re\, t_s$.

(c) Imaginärteil der Sattelpunktwirkung $\Im\, S_{\mathbf{ps}}$ vs Ionisationszeit $\Re\, t_s$.

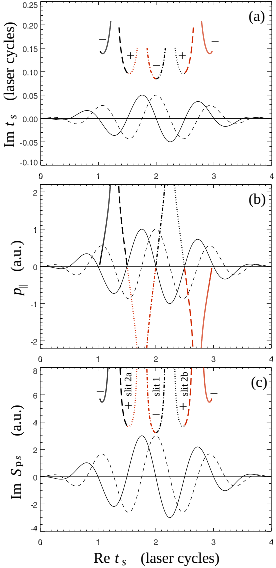

Quantenbahnen
— Beispiel I

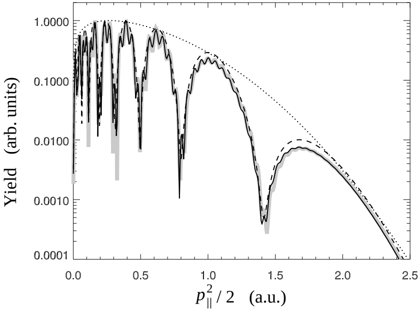

Gepunktet: nur dominierende Quantenbahn
Gestrichelt: eine weitere Bahnn
Durchgezogen: zwei weitere Bahnen
Grau: “volles” Matrixelement

G.G. Paulus and D. Bauer, in: “Time in Quantum Mechanics Vol. 2” (Springer, Heidelberg, 2009)

Quantenbahnen

— Beispiel II

- 4-Zyklen-$\sin^2$-Puls, $\omega = 0.056$, $\hat{E} = -\omega \hat{A} = 0.1$, $\varphi_{\text{cep}} = \pi/2$. $A(t)$ (durchgezogen), $E(t)$ (gestrichelt).

(a) Sattelpunktzeiten t_s in der komplexen Ebene;
+/- bzgl.
$\mathbf{A}(t_s) = -p_{\parallel} \pm \mathrm{i}\sqrt{2I + p_{\perp}^2}$,
schwarz: positiver Endimpuls $p_{\parallel}$,
rot: negativer Endimpuls $p_{\parallel}$.

(b) Endimpuls $p_{\parallel}$ vs Ionisationszeit $\Re\, t_s$.

(c) Imaginärteil der Sattelpunktwirkung $\Im\, S_{\mathbf{ps}}$ vs Ionisationszeit $\Re\, t_s$.

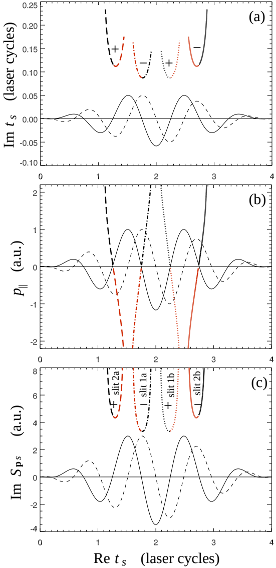

Quantenbahnen

— Beispiel II

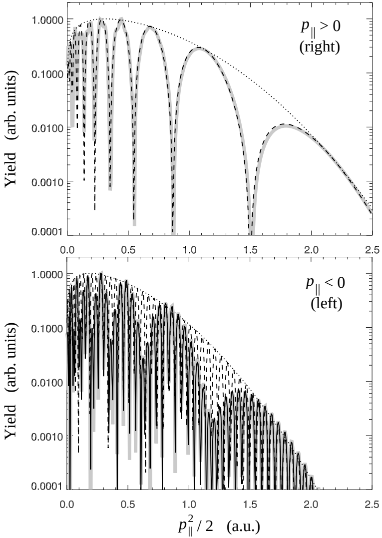

Gepunktet: nur dominierende Quantenbahn
Gestrichelt: eine weitere Bahnn
Durchgezogen: zwei weitere Bahnen
Grau: “volles” Matrixelement

G.G. Paulus and D. Bauer, in: “Time in Quantum Mechanics Vol. 2” (Springer, Heidelberg, 2009)

Bestimmung der maximalen Energie nach Rückstreuung

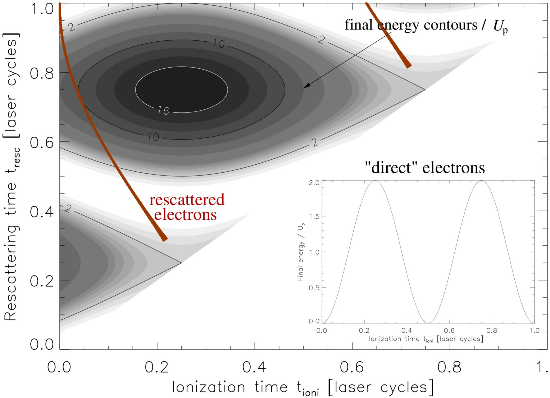

Figure 3.18: Final photoelectron energy $\mathcal{E}_{\mathrm{resc},\boldsymbol{p}}$ vs ionization time t_{ion} and rescattering time $t_{\mathrm{resc}} > t_{\mathrm{ion}}$ (black: high value of $\mathcal{E}_{\mathrm{resc},\boldsymbol{p}}$, white: small value of $\mathcal{E}_{\mathrm{resc},\boldsymbol{p}}$, contours 2, 10 and $16U_{\mathrm{p}}$ labelled explicitly). The red branch labelled "rescattered electrons" indicate times t_{ion} and t_{resc} where (3.366) is fulfilled. The highest energy those rescattered electrons can have is $10U_{\mathrm{p}}$ (see red branch touching the $10U_{\mathrm{p}}$-contour). The inlet shows the final energy (3.365) of the "direct" electrons vs the ionization time. The highest energy there is $2U_{\mathrm{p}}$.

Energie *vs* Ionisationszeit

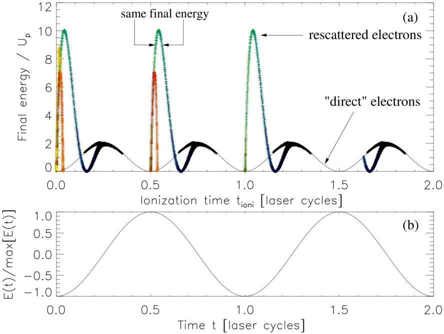

Figure 3.20: (a) Final energy of direct electrons (black line) vs the ionization time t_{ion}. If rescattered is allowed, higher energies may occur. The color coding for the rescattered electrons indicates the time spent in the continuum between ionization and rescattering, i.e., $t_{\text{resc}} - t_{\text{ion}}$ (the lighter the color the longer the time). The cut-off energies for the direct and the rescattered electrons are 2 and $10U_{\text{p}}$, respectively. Panel (b) shows the course of the laser field. Ionization is improbable for small $|E(t)|$.

Wie gut ist die SFA?

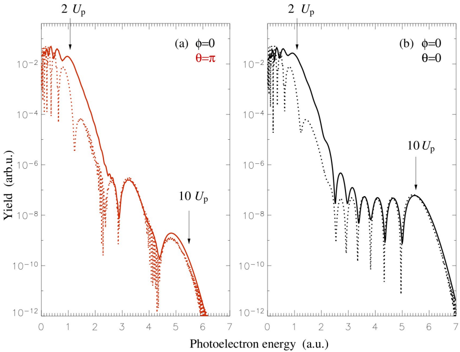

Figure 3.19: Photoelectron spectra of the H(1s) electron after irradiation with a 4-cycle laser pulse ($\omega = 0.056$, $\phi = 0$, $\hat{E} = 0.0834$). The TDSE and SFA results are drawn solid and dashed, respectively. Panel (a) shows the "left-going" electrons (i.e., opposite to the laser polarization $\boldsymbol{e}_z$), panel (b) the "right-going" electrons (in $\boldsymbol{e}_z$)-direction. The spectra were adjusted vertically by multiplication with a single factor in such a way that agreement is best in the cut-off region for the right-going electrons. The spectra were *not* shifted in energy.

Rückkehrenergien bei HOHG

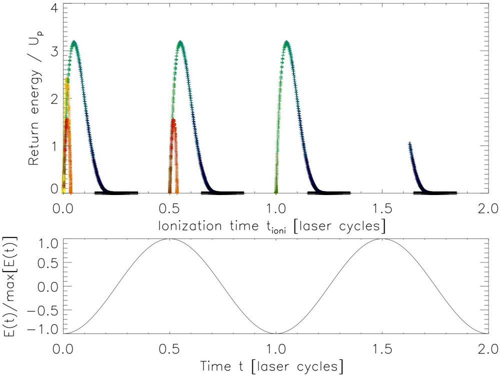

Figure 3.22: Return energy as a function of the ionization time. The color coding indicates the time between ionization and recombination (the longer this time the lighter the color). The maximum return energy is $\simeq 3.17 U_\mathrm{p}$. The course of the laser field is shown in the lower panel.

“Attosekundenkamera”

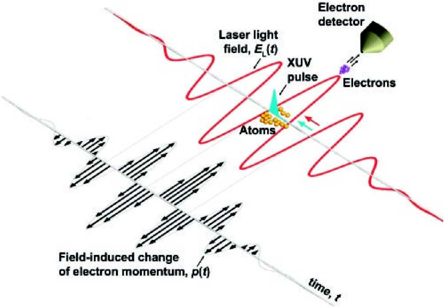

Goulielmakis *et al.*, Science **305**, 1267 (2004).

“Attosekundenkamera” ...

... “fotografiert” das elektrische Feld des Lasers mit sub-fs Auflösung

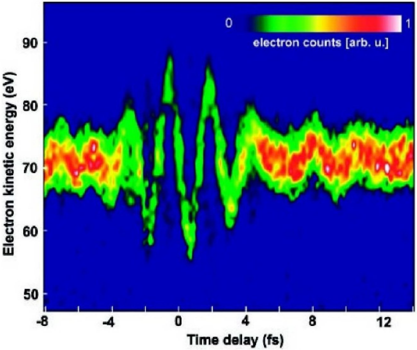

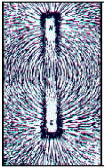

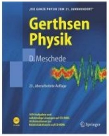

Gerthsen Physik

D. Meschede

Springer

Goulielmakis *et al.*, Science **305**, 1267 (2004).

HOHG-Spektrum aus dem Lewenstein-Modell

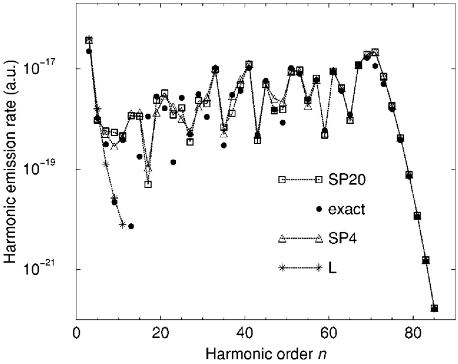

Figure 3.24: Harmonic spectrum obtained using the SFA for H(1s), 2×10^{14}Wcm^{-2}, and photon energy 1.17 eV. The time integral in (3.398) was calculated either directly (labelled "exact") or applying the saddle-point approximation. The expected cut-off at harmonic order $n = 72.3$ is confirmed. [From D.B. MILOŠEVIĆ and W. BECKER, *Role of long quantum orbits in high-order harmonic generation*, Phys. Rev. A **66**, 063417 (2002).]

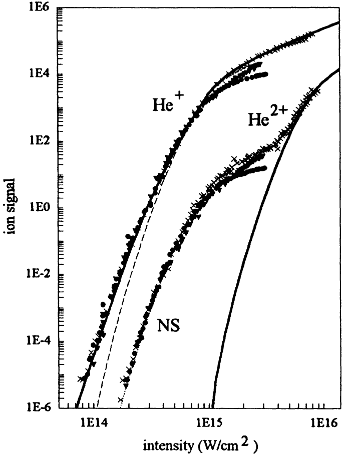

Experimental ion yields for He^{+} and He^{2+} after the interaction with a 160 fs 780 nm laser pulse. The solid lines are the theoretically expected yields when a sequential, single active electron ionization scenario is assumed [the ADK-rate was used]. It is seen that below 10^{15} Wcm^{-2} the measured He^{2+} yield is many orders of magnitude greater before it merges with the theoretical prediction. The deviation from the sequential rate (solid curve) is the so-called nonsequential ionization (NSDI) “knee.”

B. Walker *et al.*, Phys. Rev. Lett. **73**, 1227 (1994).

Reaktionsmikroskop (COLTRIMS)

Stern-Gerlach-Medaille 2010 für Horst Schmidt-Böcking, Uni Frankfurt

Philip Morris Forschungspreis 2006 für J. Ullrich & R. Moshammer, MPI-K

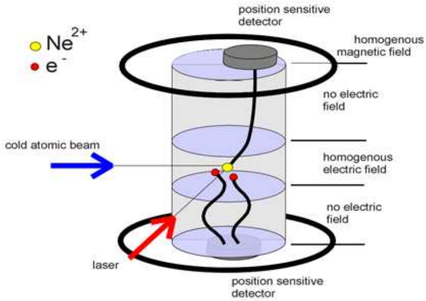

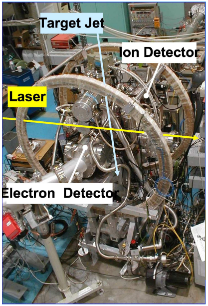

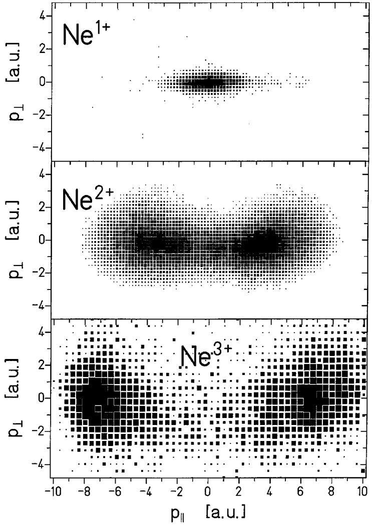

Momentum distributions of Ne^{n+} ions at 1.3 PWcm^{-2} (Ne^{+}, Ne^{2+}) and 1.5 PWcm^{-2} (Ne^{3+}) after a 30 fs 795 nm laser pulse obtained with the COLTRIMS method. $p_\parallel$ is the momentum parallel to the laser polarization, $p_\perp$ perpendicular to it. The distribution for Ne^{2+} and Ne^{3+} shows a minimum at $p_\parallel$, indicating that NSDI is not a (pure) shake-off effect but relies on Coulomb interaction of the electrons.

R. Moshammer *et al.*, Phys. Rev. Lett. **84**, 447 (2000).

Ion momentum spectra: the “double hump”

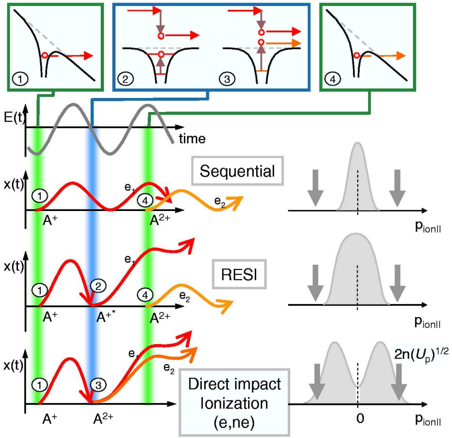

- Recollision-induced excitation followed by subsequent field ionization (RESI)
- Nonsequential multiple ionization (NSMI) [“direct impact ionization” (*e*, *ne*)]

A. Rudenko *et al.*, Phys. Rev. Lett. **93**, 253001 (2004)

Ion momentum spectra: the “double hump”

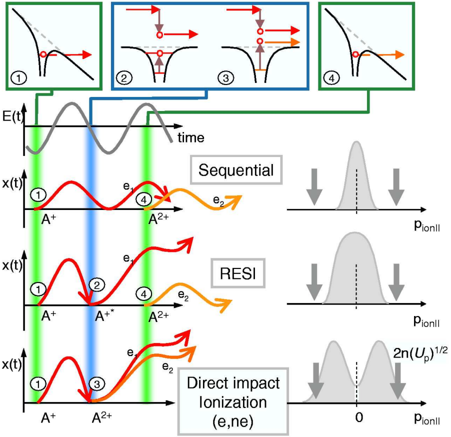

- Recollision-induced excitation followed by subsequent field ionization (RESI)
- Nonsequential multiple ionization (NSMI) [“direct impact ionization” (*e*, *ne*)]

A. Rudenko *et al.*, Phys. Rev. Lett. **93**, 253001 (2004)

Ion momentum spectra: the “double hump”

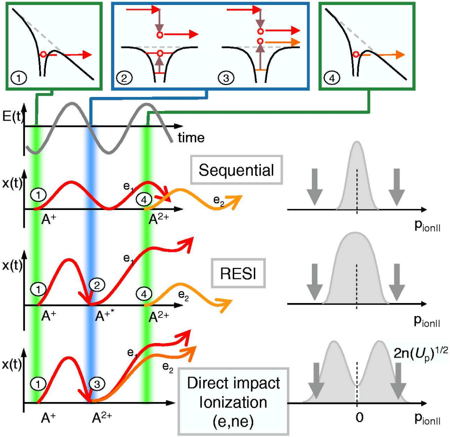

- Recollision-induced excitation followed by subsequent field ionization (RESI)
- Nonsequential multiple ionization (NSMI) [“direct impact ionization” (*e*, *ne*)]

A. Rudenko *et al.*, Phys. Rev. Lett. **93**, 253001 (2004)

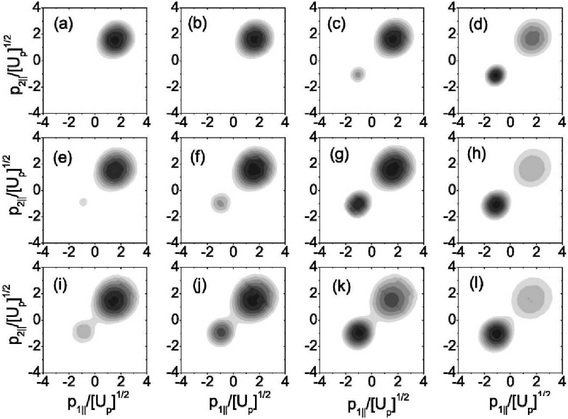

Differential electron momentum distributions computed for neon ($\mathcal{E}_{01} = -0.79$ and $\mathcal{E}_{02} = -1.51$ a.u.) subject to a fourcycle pulse of frequency $\omega = 0.057$ (Ti:Sapphire, $\lambda \simeq 800$ nm) and various intensities and absolute phases. The upper, middle and lower panels correspond to $I = 4 \cdot 10^{14}$ Wcm^{-2} ($U_{\rm p} = 0.879$), $I = 5.5 \cdot 10^{14}$ Wcm^{-2} ($U_{\rm p} = 1.2$), and $I = 8 \cdot 10^{14}$ Wcm^{-2} ($U_{\rm p} = 1.758$), respectively. The absolute phases are given as follows: Panels (a), (e), and (i): $\phi = 0.8\pi$; panels (b), (f), and (j): $\phi = 0.9\pi$; panels (c), (g), and (k): $\phi = \pi$; and panels (d), (h), and (l): $\phi = 1.1\pi$.

C. Figueira de Morisson Faria *et al.*, Phys. Rev. A **70**, 043406 (2004).

Ne atom, DFT calculations

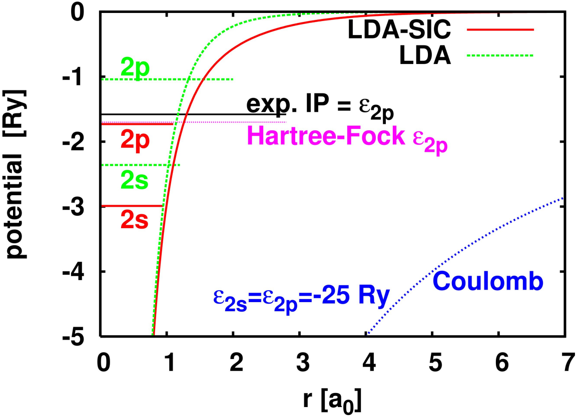

Obenstehendes Bild illustriert LDA am Beispiel des Neon-Atoms (Kernladungszahl $N = 10$). Es zeigt die Gesamtpotentiale für LDA, LDA-SIC sowie reines Coulomb und dazu jeweils die Einteilchenenergien als horizontale Linien. Die Zuordnung geschieht über die Farbe (grün = LDA, rot = LDA mit SIC, blau = reines Kern-Coulombfeld, schwarz = experimenteller Wert, lila = Hartree-Fock-Resultat).

von P.-G. Reinhard, Uni Erlangen-Nürnberg

TDDFT: Lineare Antwort von C_{60}

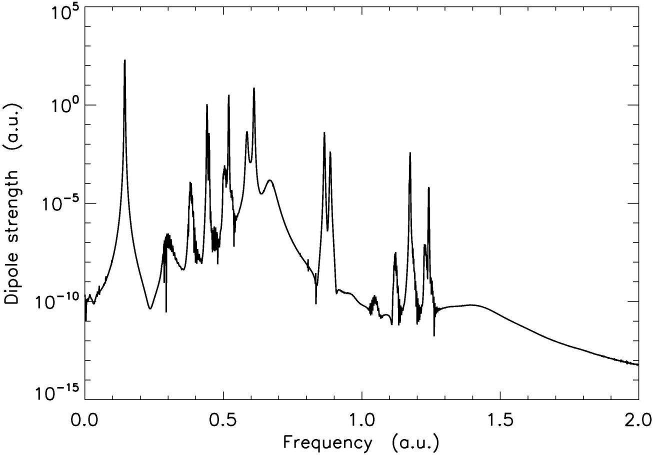

Interpretation von ω_{Mie} und ω_{p} als Einteilchenübergänge

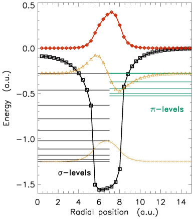

$\sigma \rightarrow \delta$

$$\sigma\ell \rightarrow \pi(\ell+1),\ \pi\ell \rightarrow \sigma(\ell-1)$$

$$\sigma\ell \rightarrow \pi(\ell-1),\ \pi\ell \rightarrow \sigma(\ell+1)$$

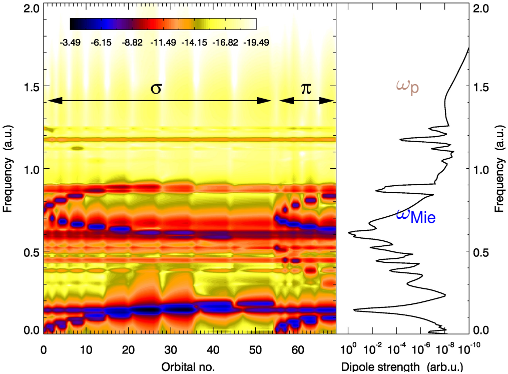

Topological aspects of a fluid description

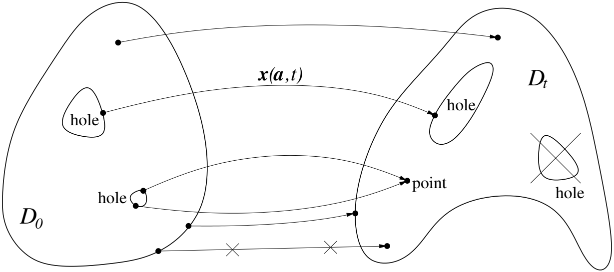

Topological aspects of a fluid description

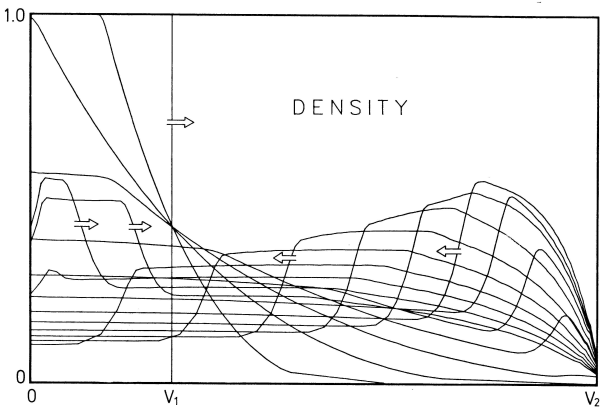

Gay-Lussac

PIC-Study of Harmonic Generation

Normal incidence, moderate intensity

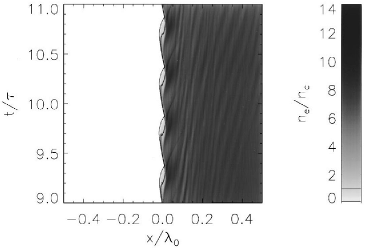

FIG. 2. Electron density $n(x,t)$ given by a grey scale in units of the critical density n_c versus coordinate x and time t in units of laser wavelength λ_0 and cycle time τ. A laser pulse with linear polarization and maximum intensity $I\lambda_0^2=3.4\times10^{17}$ W cm$^{-2}\mu$m^2 ($a_0=0.5$) is normally incident on the uniform layer with density $n_0/n_c=7$. The intensity varies $\propto \sin^4(\pi t/T)$ with pulse duration $T=20\tau$. The time window shown corresponds to two cycles around the pulse maximum. The initial surface position is $x/\lambda_0=0$. The contour lines mark the critical density $n=n_c$ and $n=0.1n_c$, respectively.

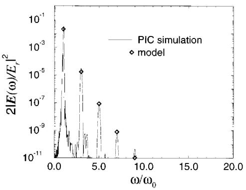

FIG. 3. Harmonic spectrum for the case of Fig. 2 with parameters: $a_0=0.5$, $n_0/n_c=7$, $\alpha=0$, linear polarization. Scaled intensity is plotted versus scaled frequency; for details see Section III. The diamonds refer to the oscillating mirror model with $X(t)=-0.011\lambda_0\cos(2\omega_0 t)$; see Section VII.

R. Lichters, J. Meyer-ter-Vehn, and A. Pukhov, Phys. Plasmas **3**, 3425 (1996)

PIC-Study of Harmonic Generation

Normal incidence, moderate intensity, lower density

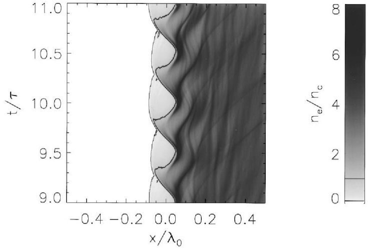

FIG. 4. Electron density for parameters: $a_0=0.5$, $n_0/n_c=4$, $\alpha=0$, linear polarization.

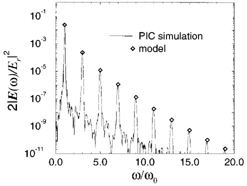

FIG. 5. Spectrum corresponding to the case of Fig. 4; the diamonds refer to the model with $X(t)=-0.033\lambda_0\cos(2\omega_0 t-\pi/2)$.

R. Lichters, J. Meyer-ter-Vehn, and A. Pukhov, Phys. Plasmas **3**, 3425 (1996)

PIC-Study of Harmonic Generation

Normal incidence, higher intensity, lower density

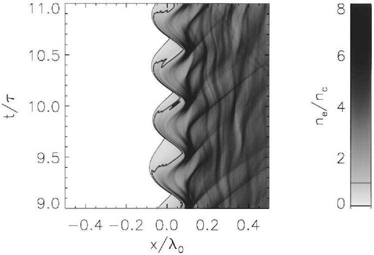

FIG. 6. Electron density for parameters: $a_0=1$, $n_0/n_c=4$, $\alpha=0$, linear polarization.

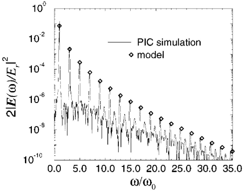

FIG. 7. Spectrum corresponding to the case of Fig. 6; the diamonds refer to the model with $X(t)=-0.052\lambda_0\cos(2\omega_0 t-\pi/2)$.

R. Lichters, J. Meyer-ter-Vehn, and A. Pukhov, Phys. Plasmas **3**, 3425 (1996)

PIC-Study of Harmonic Generation

Oblique incidence, s-pol.

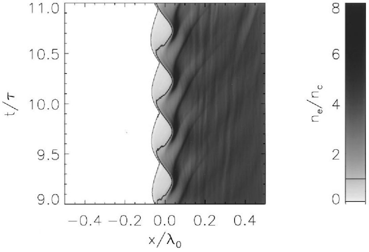

FIG. 8. Electron density for oblique incidence of *s*-polarized light with parameters: $a_0=0.5$, $n_0/n_c=4$, $\alpha=30°$.

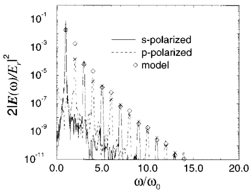

FIG. 9. Spectrum corresponding to the case of Fig. 8; the diamonds refer to the model with $X(t) = -0.023\lambda_0\cos(2(\omega_0\cos\alpha)t-\pi/2)$ and the crosses to the modified model explained in Section VIIC.

R. Lichters, J. Meyer-ter-Vehn, and A. Pukhov, Phys. Plasmas **3**, 3425 (1996)

PIC-Study of Harmonic Generation

Oblique incidence, p-pol.

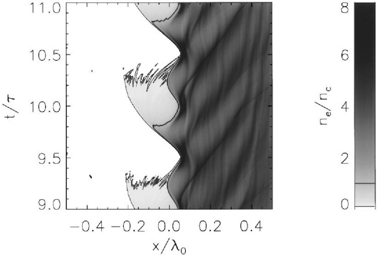

FIG. 10. Electron density for oblique incidence of *p*-polarized light with parameters: $a_0=0.5$, $n_0/n_c=4$, $\alpha=30°$.

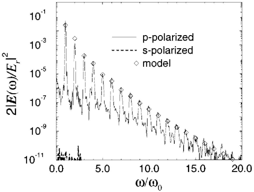

FIG. 11. Spectrum corresponding to the case of Fig. 10; diamonds refer to $X(t)=+0.027\lambda_0 \sin((\omega_0 \cos\alpha)t) - 0.023\lambda_0 \cos(2(\omega_0 \cos\alpha)t - \pi/2)$ and $\alpha=30°$.

R. Lichters, J. Meyer-ter-Vehn, and A. Pukhov, Phys. Plasmas **3**, 3425 (1996)

PIC-Study of Radiation Pressure Acceleration

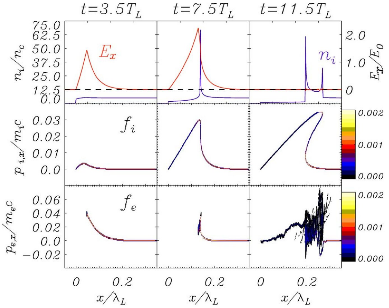

Fig. 1. One-dimensional PIC simulation of the interaction of a short CP laser pulse with an overdense step-boundary plasma. The figure shows the (top row, solid line) ion density n_i, (top row, dotted) electrostatic field E_x, and (x, p_x) phase-space distribution for (middle row) ions f_i and (bottom row) electrons f_e at different times in laser cycles. For a laser wavelength $\lambda_L = 1\ \mu\text{m}$, the laser and plasma parameters correspond to an irradiance $I\lambda_L^2 = 5.5 \times 10^{18}\ \text{W} \cdot \mu\text{m}^2/\text{cm}^2$, a pulse duration $\tau_L = 20$ fs, and an initial electron density $n_e = 5.5 \times 10^{21}\ \text{cm}^{-3}$. The x-coordinate is normalized to $\lambda_L = 1\ \mu\text{m}$, the density to $n_c = 1.1 \times 10^{21}\ \text{cm}^{-3}$, and the momenta to $m_e c$ and $m_i c$, respectively. The electric field is normalized to $E_n = m_e \omega_L c/e$.

T.V. Liseikina *et al.*, IEEE Transactions on Plasma Science **36**, 1866 (2008)

PIC-Study of Radiation Pressure Acceleration

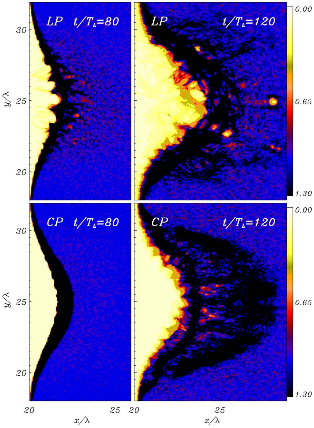

Fig. 6. Contours of the ion density from 2-D simulation results for CP and LP at two different times, showing the growth of surface rippling at the laser-irradiated surface. Simulation parameters are the same as in Fig. 5.

T.V. Liseikina *et al.*, IEEE Transactions on Plasma Science **36**, 1866 (2008)

Elektronenbeschleunigung ...

... im Unterdichten:

“wake field acceleration”

news and views

Electrons hang ten on laser wake

Thomas Katsouleas

Electrons can be accelerated by making them surf a laser-driven plasma wave. High acceleration rates, and now the production of well-populated, high-quality beams, signal the potential of this table-top technology.

Nature **431**, (2004)

10^9 Elektronen, 10 fs
von 0 auf $\simeq$ 100 MeV über 1 mm,
kleine Strahldivergenz, 10% Energiebreite

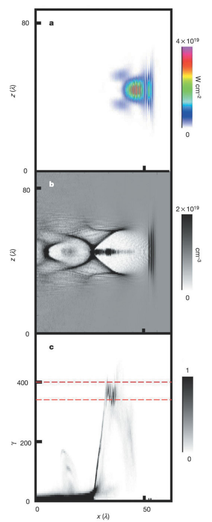

PIC-Rechnung von A. Pukhov

3D, relativistic particle-in-cell simulations

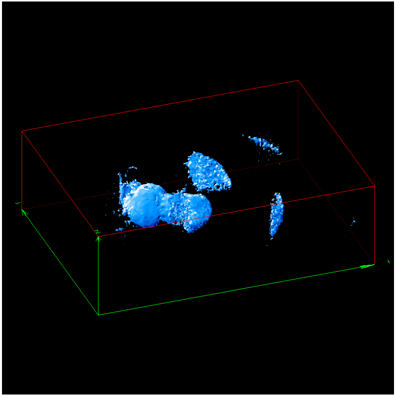

He-droplet, $R = 0.25\,\lambda$
$\lambda = 800\,\text{nm}$, 16 Zyklen $\sin^2$
$a = 1$ ($I \simeq 2 \times 10^{18}\,\text{Wcm}^{-2}$)
$n_{e0} = 22\,n_c$,
$n_c = 1.8 \times 10^{21}\,\text{cm}^{-3}$
$t = 8$ Zyklen
1% n_{e0}-isocontour

3D, relativistic particle-in-cell simulations

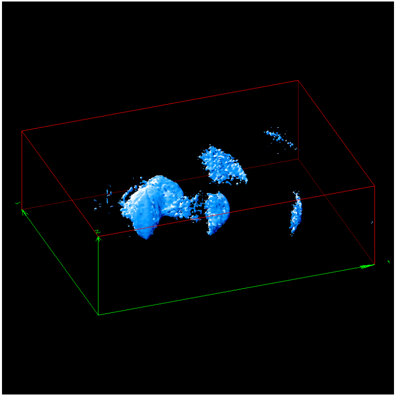

He-droplet, $R = 0.25\,\lambda$
$\lambda = 800\,\text{nm}$, 16 Zyklen $\sin^2$
$a = 1$ ($I \simeq 2 \times 10^{18}\,\text{Wcm}^{-2}$)
$n_{e0} = 22\,n_c$,
$n_c = 1.8 \times 10^{21}\,\text{cm}^{-3}$
$t = 8.25$ Zyklen
1% n_{e0}-isocontour

3D, relativistic particle-in-cell simulations

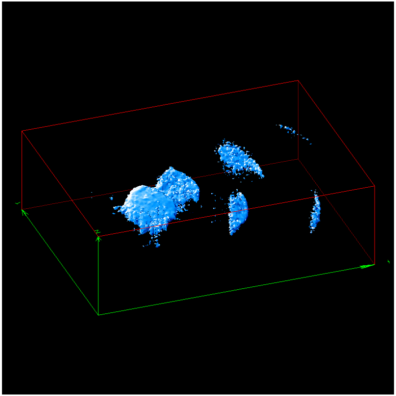

He-droplet, $R = 0.25\,\lambda$

$\lambda = 800\,\mathrm{nm}$, 16 Zyklen $\sin^2$

$a = 1$ ($I \simeq 2 \times 10^{18}\,\mathrm{Wcm^{-2}}$)

$n_{e0} = 22\,n_c$,

$n_c = 1.8 \times 10^{21}\,\mathrm{cm^{-3}}$

$t = 8.5$ Zyklen

1% n_{e0}-isocontour

3D, relativistic particle-in-cell simulations

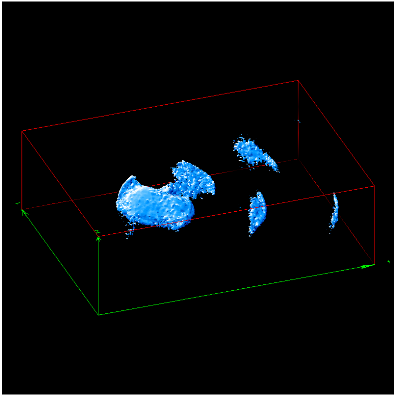

He-droplet, $R = 0.25\,\lambda$
$\lambda = 800\,\text{nm}$, 16 Zyklen $\sin^2$
$a = 1$ ($I \simeq 2 \times 10^{18}\,\text{Wcm}^{-2}$)
$n_{e0} = 22\,n_c$,
$n_c = 1.8 \times 10^{21}\,\text{cm}^{-3}$
$t = 8.75$ Zyklen
1% n_{e0}-isocontour

3D, relativistic particle-in-cell simulations

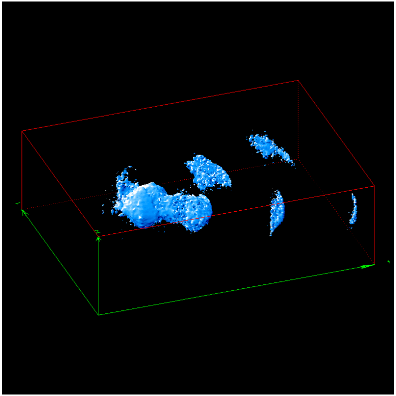

He-droplet, $R = 0.25\,\lambda$
$\lambda = 800\,\mathrm{nm}$, 16 Zyklen $\sin^2$
$a = 1$ ($I \simeq 2 \times 10^{18}\,\mathrm{Wcm}^{-2}$)
$n_{e0} = 22\,n_c$,
$n_c = 1.8 \times 10^{21}\,\mathrm{cm}^{-3}$
$t = 9$ Zyklen
1% n_{e0}-isocontour

3D, relativistic particle-in-cell simulations

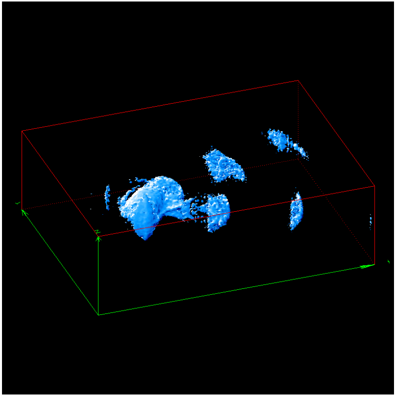

He-droplet, $R = 0.25\,\lambda$
$\lambda = 800\,\text{nm}$, 16 Zyklen $\sin^2$
$a = 1$ ($I \simeq 2 \times 10^{18}\,\text{Wcm}^{-2}$)
$n_{e0} = 22\,n_c$,
$n_c = 1.8 \times 10^{21}\,\text{cm}^{-3}$
$t = 9.25$ Zyklen
1% n_{e0}-isocontour

3D, relativistic particle-in-cell simulations

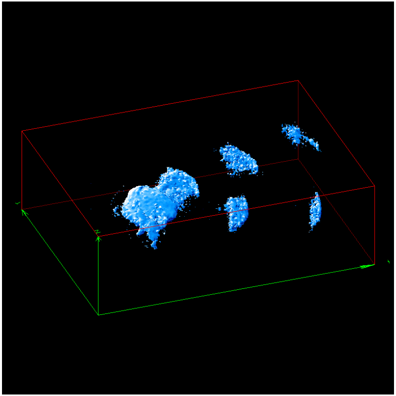

He-droplet, $R = 0.25\,\lambda$
$\lambda = 800\,\mathrm{nm}$, 16 Zyklen $\sin^2$
$a = 1$ ($I \simeq 2 \times 10^{18}\,\mathrm{Wcm}^{-2}$)
$n_{e0} = 22\,n_c$,
$n_c = 1.8 \times 10^{21}\,\mathrm{cm}^{-3}$
$t = 9.50$ Zyklen
1% n_{e0}-isocontour

3D, relativistic particle-in-cell simulations

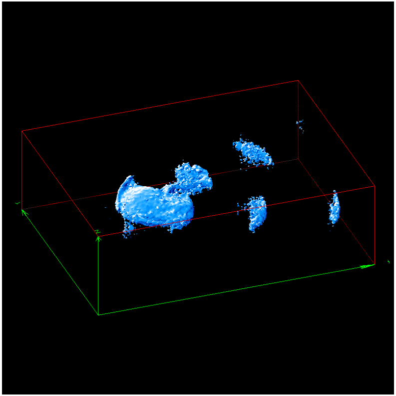

He-droplet, $R = 0.25\,\lambda$

$\lambda = 800\,\text{nm}$, 16 Zyklen $\sin^2$

$a = 1$ ($I \simeq 2 \times 10^{18}\,\text{Wcm}^{-2}$)

$n_{e0} = 22\,n_c$,

$n_c = 1.8 \times 10^{21}\,\text{cm}^{-3}$

$t = 9.75$ Zyklen

1% n_{e0}-isocontour

3D, relativistic particle-in-cell simulations

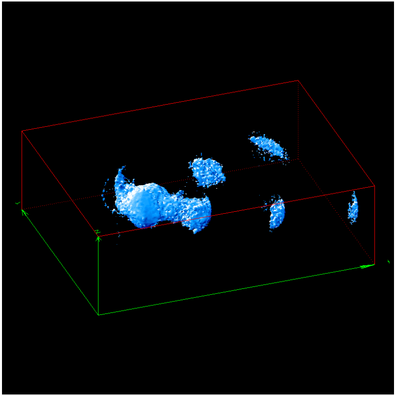

He-droplet, $R = 0.25\,\lambda$
$\lambda = 800\,\mathrm{nm}$, 16 Zyklen $\sin^2$
$a = 1$ ($I \simeq 2 \times 10^{18}\,\mathrm{Wcm}^{-2}$)
$n_{e0} = 22\,n_c$,
$n_c = 1.8 \times 10^{21}\,\mathrm{cm}^{-3}$
$t = 10$ Zyklen
1% n_{e0}-isocontour

Elektronenenergien und -dichten

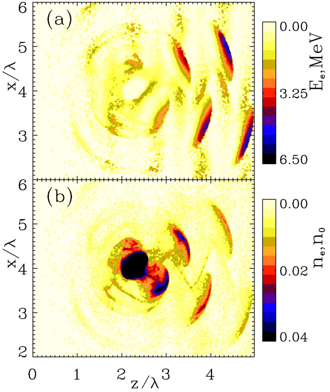

He-droplet, $R = 0.25\,\lambda$
$\lambda = 800\,\text{nm}$, 16 Zyklen $\sin^2$
$a = 2$ ($I \simeq 8 \times 10^{18}\,\text{Wcm}^{-2}$)
$n_{e0} = 22\,n_c$,
$n_c = 1.8 \times 10^{21}\,\text{cm}^{-3}$
$t = 8$ Zyklen

6 MeV
Attosekunden-Elektronenpulse

$$U_\text{p} = mc^2 \left[\sqrt{1 + \frac{a^2}{2}} - 1\right]$$

nur $\simeq 0.4\,\text{MeV}$

T.V. Liseykina, S. Pirner, and D. Bauer, Phys. Rev. Lett. (accepted)

3D, relativistic particle-in-cell simulations

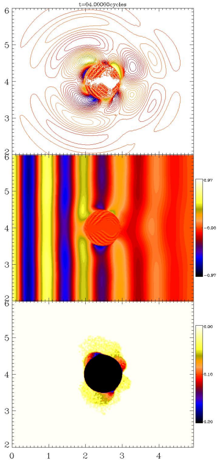

Felder $\mathbf{E} \parallel \mathbf{k}$, $\mathbf{E} \parallel \mathbf{E}_{\text{inc}}$ und Dichte

He-droplet, $R = 0.5\,\lambda$
$\lambda = 800\,\text{nm}$, 16 Zyklen $\sin^2$
$a = 1.0$ ($I \simeq 2 \times 10^{18}\,\text{Wcm}^{-2}$)
$n_{e0} = 22\,n_c$, $n_c = 1.8 \times 10^{21}\,\text{cm}^{-3}$
$t = 4.0$ Zyklen

3D, relativistic particle-in-cell simulations

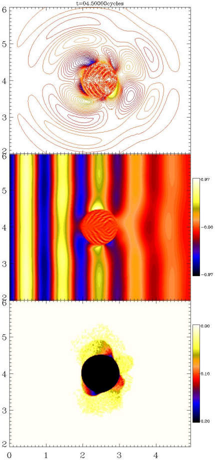

Felder $\mathbf{E} \parallel \mathbf{k}$, $\mathbf{E} \parallel \mathbf{E}_{\mathrm{inc}}$ und Dichte

He-droplet, $R = 0.5\,\lambda$
$\lambda = 800\,\mathrm{nm}$, 16 Zyklen $\sin^2$
$a = 1.0$ ($I \simeq 2 \times 10^{18}\,\mathrm{Wcm}^{-2}$)
$n_{e0} = 22\,n_c$, $n_c = 1.8 \times 10^{21}\,\mathrm{cm}^{-3}$
$t = 4.5$ Zyklen

3D, relativistic particle-in-cell simulations

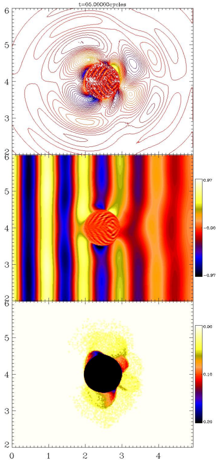

Felder $\mathbf{E} \parallel \mathbf{k}$, $\mathbf{E} \parallel \mathbf{E}_{\text{inc}}$ und Dichte

He-droplet, $R = 0.5\,\lambda$
$\lambda = 800\,\text{nm}$, 16 Zyklen $\sin^2$
$a = 1.0$ ($I \simeq 2 \times 10^{18}\,\text{Wcm}^{-2}$)
$n_{e0} = 22\,n_c$, $n_c = 1.8 \times 10^{21}\,\text{cm}^{-3}$
$t = 5.0$ Zyklen

3D, relativistic particle-in-cell simulations

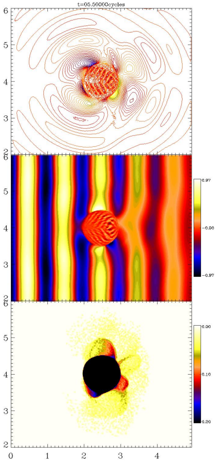

Felder $\mathbf{E} \parallel \mathbf{k}$, $\mathbf{E} \parallel \mathbf{E}_{\text{inc}}$ und Dichte

He-droplet, $R = 0.5\,\lambda$
$\lambda = 800\,\text{nm}$, 16 Zyklen $\sin^2$
$a = 1.0$ ($I \simeq 2 \times 10^{18}\,\text{Wcm}^{-2}$)
$n_{e0} = 22\,n_c$, $n_c = 1.8 \times 10^{21}\,\text{cm}^{-3}$
$t = 5.5$ Zyklen

3D, relativistic particle-in-cell simulations

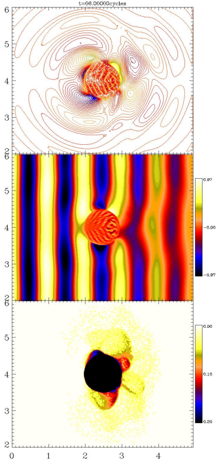

Felder $\mathbf{E} \parallel \mathbf{k}$, $\mathbf{E} \parallel \mathbf{E}_{\text{inc}}$ und Dichte

He-droplet, $R = 0.5\,\lambda$
$\lambda = 800\,\text{nm}$, 16 Zyklen $\sin^2$
$a = 1.0$ ($I \simeq 2 \times 10^{18}\,\text{Wcm}^{-2}$)
$n_{e0} = 22\,n_c$, $n_c = 1.8 \times 10^{21}\,\text{cm}^{-3}$
$t = 6.0$ Zyklen

3D, relativistic particle-in-cell simulations

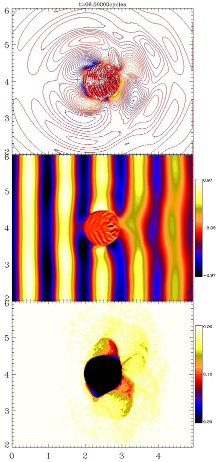

Felder $\mathbf{E} \parallel \mathbf{k}$, $\mathbf{E} \parallel \mathbf{E}_{\text{inc}}$ und Dichte

He-droplet, $R = 0.5\,\lambda$
$\lambda = 800\,\text{nm}$, 16 Zyklen $\sin^2$
$a = 1.0$ ($I \simeq 2 \times 10^{18}\,\text{Wcm}^{-2}$)
$n_{e0} = 22\,n_c$, $n_c = 1.8 \times 10^{21}\,\text{cm}^{-3}$
$t = 6.5$ Zyklen

3D, relativistic particle-in-cell simulations

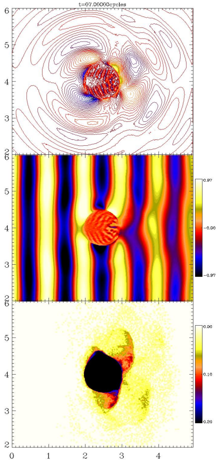

Felder $\mathbf{E} \parallel \mathbf{k}$, $\mathbf{E} \parallel \mathbf{E}_{\text{inc}}$ und Dichte

He-droplet, $R = 0.5\,\lambda$
$\lambda = 800\,\text{nm}$, 16 Zyklen $\sin^2$
$a = 1.0$ ($I \simeq 2 \times 10^{18}\,\text{Wcm}^{-2}$)
$n_{e0} = 22\,n_c$, $n_c = 1.8 \times 10^{21}\,\text{cm}^{-3}$
$t = 7.0$ Zyklen

3D, relativistic particle-in-cell simulations

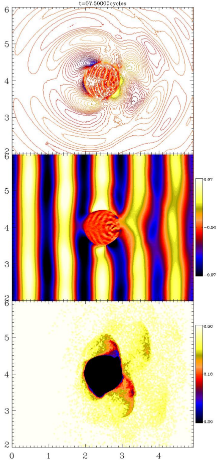

Felder $\mathbf{E} \parallel \mathbf{k}$, $\mathbf{E} \parallel \mathbf{E}_{\mathrm{inc}}$ und Dichte

He-droplet, $R = 0.5\,\lambda$
$\lambda = 800\,\mathrm{nm}$, 16 Zyklen $\sin^2$
$a = 1.0$ ($I \simeq 2 \times 10^{18}\,\mathrm{Wcm}^{-2}$)
$n_{e0} = 22\,n_c$, $n_c = 1.8 \times 10^{21}\,\mathrm{cm}^{-3}$
$t = 7.5$ Zyklen

3D, relativistic particle-in-cell simulations

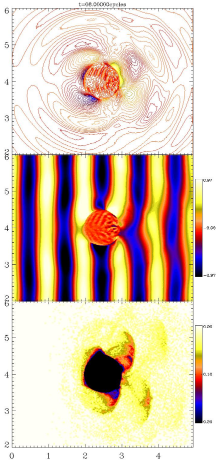

Felder **E** $\parallel$ **k**, **E** $\parallel$ $\mathbf{E}_{\text{inc}}$ und Dichte

He-droplet, $R = 0.5\,\lambda$
$\lambda = 800\,\text{nm}$, 16 Zyklen $\sin^2$
$a = 1.0$ ($I \simeq 2 \times 10^{18}\,\text{Wcm}^{-2}$)
$n_{e0} = 22\,n_c$, $n_c = 1.8 \times 10^{21}\,\text{cm}^{-3}$
$t = 8.0$ Zyklen

3D, relativistic particle-in-cell simulations

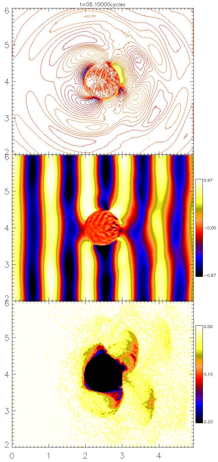

Felder $\mathbf{E} \parallel \mathbf{k}$, $\mathbf{E} \parallel \mathbf{E}_{\text{inc}}$ und Dichte

He-droplet, $R = 0.5\,\lambda$
$\lambda = 800\,\text{nm}$, 16 Zyklen $\sin^2$
$a = 1.0$ ($I \simeq 2 \times 10^{18}\,\text{Wcm}^{-2}$)
$n_{e0} = 22\,n_c$, $n_c = 1.8 \times 10^{21}\,\text{cm}^{-3}$
$t = 8.1$ Zyklen

3D, relativistic particle-in-cell simulations

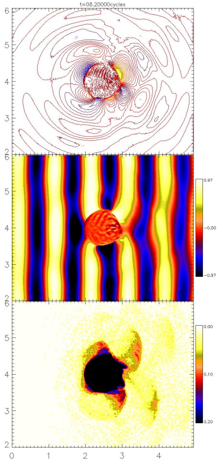

Felder **E** $\parallel$ **k**, **E** $\parallel$ $\mathbf{E}_{\text{inc}}$ und Dichte

He-droplet, $R = 0.5\,\lambda$
$\lambda = 800\,\text{nm}$, 16 Zyklen $\sin^2$
$a = 1.0$ ($I \simeq 2 \times 10^{18}\,\text{Wcm}^{-2}$)
$n_{e0} = 22\,n_c$, $n_c = 1.8 \times 10^{21}\,\text{cm}^{-3}$
$t = 8.2$ Zyklen

3D, relativistic particle-in-cell simulations

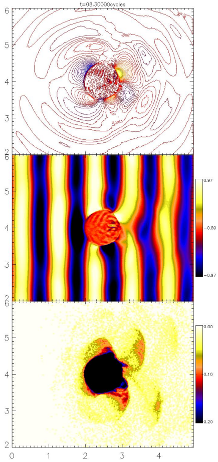

Felder $\mathbf{E} \parallel \mathbf{k}$, $\mathbf{E} \parallel \mathbf{E}_{\mathrm{inc}}$ und Dichte

He-droplet, $R = 0.5\,\lambda$
$\lambda = 800\,\mathrm{nm}$, 16 Zyklen $\sin^2$
$a = 1.0$ ($I \simeq 2 \times 10^{18}\,\mathrm{Wcm}^{-2}$)
$n_{e0} = 22\,n_c$, $n_c = 1.8 \times 10^{21}\,\mathrm{cm}^{-3}$
$t = 8.3$ Zyklen

3D, relativistic particle-in-cell simulations

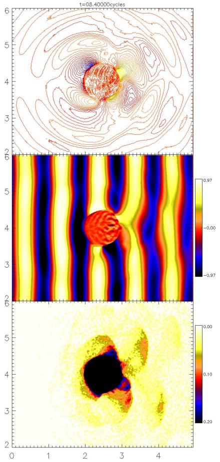

Felder $\mathbf{E} \parallel \mathbf{k}$, $\mathbf{E} \parallel \mathbf{E}_{\text{inc}}$ und Dichte

He-droplet, $R = 0.5\,\lambda$
$\lambda = 800\,\text{nm}$, 16 Zyklen $\sin^2$
$a = 1.0$ ($I \simeq 2 \times 10^{18}\,\text{Wcm}^{-2}$)
$n_{e0} = 22\,n_c$, $n_c = 1.8 \times 10^{21}\,\text{cm}^{-3}$
$t = 8.4$ Zyklen

3D, relativistic particle-in-cell simulations

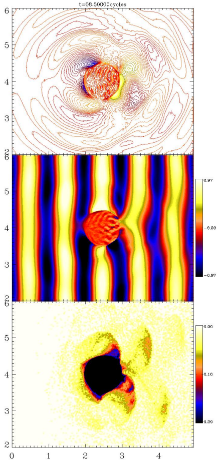

Felder $\mathbf{E} \parallel \mathbf{k}$, $\mathbf{E} \parallel \mathbf{E}_{\mathrm{inc}}$ und Dichte

He-droplet, $R = 0.5\,\lambda$
$\lambda = 800\,\mathrm{nm}$, 16 Zyklen $\sin^2$
$a = 1.0$ ($I \simeq 2 \times 10^{18}\,\mathrm{Wcm}^{-2}$)
$n_{e0} = 22\,n_c$, $n_c = 1.8 \times 10^{21}\,\mathrm{cm}^{-3}$
$t = 8.5$ Zyklen

3D, relativistic particle-in-cell simulations

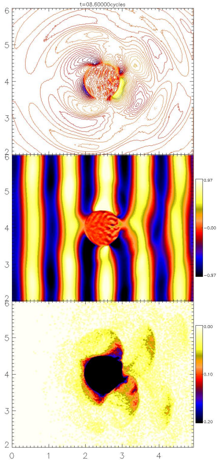

Felder $\mathbf{E} \parallel \mathbf{k}$, $\mathbf{E} \parallel \mathbf{E}_{\mathrm{inc}}$ und Dichte

He-droplet, $R = 0.5\,\lambda$
$\lambda = 800\,\mathrm{nm}$, 16 Zyklen $\sin^2$
$a = 1.0$ ($I \simeq 2 \times 10^{18}\,\mathrm{Wcm}^{-2}$)
$n_{e0} = 22\,n_c$, $n_c = 1.8 \times 10^{21}\,\mathrm{cm}^{-3}$
$t = 8.6$ Zyklen

3D, relativistic particle-in-cell simulations

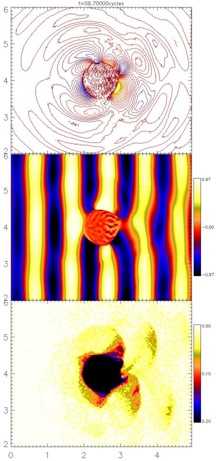

Felder $\mathbf{E} \parallel \mathbf{k}$, $\mathbf{E} \parallel \mathbf{E}_{\text{inc}}$ und Dichte

He-droplet, $R = 0.5\,\lambda$
$\lambda = 800\,\text{nm}$, 16 Zyklen $\sin^2$
$a = 1.0$ ($I \simeq 2 \times 10^{18}\,\text{Wcm}^{-2}$)
$n_{e0} = 22\,n_c$, $n_c = 1.8 \times 10^{21}\,\text{cm}^{-3}$
$t = 8.7$ Zyklen

3D, relativistic particle-in-cell simulations

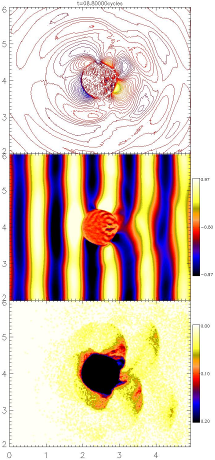

Felder $\mathbf{E} \parallel \mathbf{k}$, $\mathbf{E} \parallel \mathbf{E}_{\text{inc}}$ und Dichte

He-droplet, $R = 0.5\,\lambda$
$\lambda = 800\,\text{nm}$, 16 Zyklen $\sin^2$
$a = 1.0$ ($I \simeq 2 \times 10^{18}\,\text{Wcm}^{-2}$)
$n_{e0} = 22\,n_c$, $n_c = 1.8 \times 10^{21}\,\text{cm}^{-3}$
$t = 8.8$ Zyklen

3D, relativistic particle-in-cell simulations

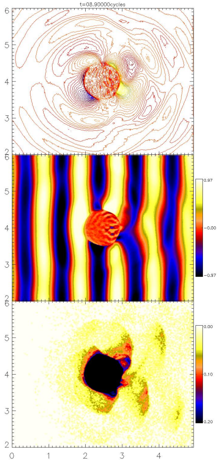

Felder $\mathbf{E} \parallel \mathbf{k}$, $\mathbf{E} \parallel \mathbf{E}_{\mathrm{inc}}$ und Dichte

He-droplet, $R = 0.5\,\lambda$
$\lambda = 800\,\mathrm{nm}$, 16 Zyklen $\sin^2$
$a = 1.0$ ($I \simeq 2 \times 10^{18}\,\mathrm{Wcm}^{-2}$)
$n_{e0} = 22\,n_c$, $n_c = 1.8 \times 10^{21}\,\mathrm{cm}^{-3}$
$t = 8.9$ Zyklen

3D, relativistic particle-in-cell simulations

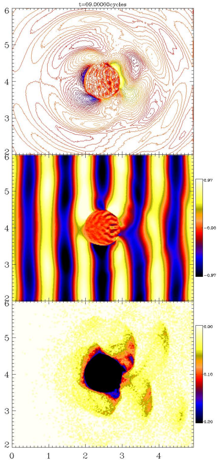

Felder $\mathbf{E} \parallel \mathbf{k}$, $\mathbf{E} \parallel \mathbf{E}_{\text{inc}}$ und Dichte

He-droplet, $R = 0.5\,\lambda$
$\lambda = 800\,\text{nm}$, 16 Zyklen $\sin^2$
$a = 1.0$ ($I \simeq 2 \times 10^{18}\,\text{Wcm}^{-2}$)
$n_{e0} = 22\,n_c$, $n_c = 1.8 \times 10^{21}\,\text{cm}^{-3}$
$t = 9.0$ Zyklen

3D, relativistic particle-in-cell simulations

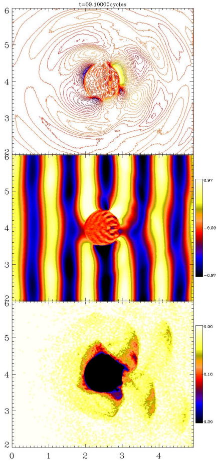

Felder $\mathbf{E} \parallel \mathbf{k}$, $\mathbf{E} \parallel \mathbf{E}_{\mathrm{inc}}$ und Dichte

He-droplet, $R = 0.5\,\lambda$
$\lambda = 800\,\mathrm{nm}$, 16 Zyklen $\sin^2$
$a = 1.0$ ($I \simeq 2 \times 10^{18}\,\mathrm{Wcm}^{-2}$)
$n_{e0} = 22\,n_c$, $n_c = 1.8 \times 10^{21}\,\mathrm{cm}^{-3}$
$t = 9.1$ Zyklen

3D, relativistic particle-in-cell simulations

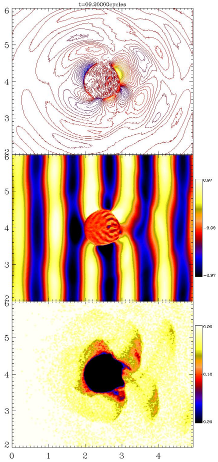

Felder $\mathbf{E} \parallel \mathbf{k}$, $\mathbf{E} \parallel \mathbf{E}_{\mathrm{inc}}$ und Dichte

He-droplet, $R = 0.5\,\lambda$
$\lambda = 800\,\mathrm{nm}$, 16 Zyklen $\sin^2$
$a = 1.0$ ($I \simeq 2 \times 10^{18}\,\mathrm{Wcm}^{-2}$)
$n_{e0} = 22\,n_c$, $n_c = 1.8 \times 10^{21}\,\mathrm{cm}^{-3}$
$t = 9.2$ Zyklen

3D, relativistic particle-in-cell simulations

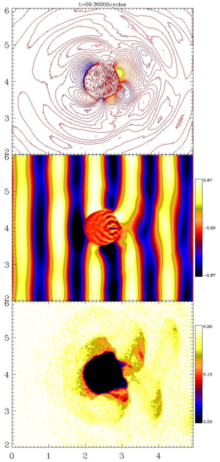

Felder **E** $\parallel$ **k**, **E** $\parallel$ $\mathbf{E}_{\text{inc}}$ und Dichte

He-droplet, $R = 0.5\,\lambda$
$\lambda = 800\,\text{nm}$, 16 Zyklen $\sin^2$
$a = 1.0$ ($I \simeq 2 \times 10^{18}\,\text{Wcm}^{-2}$)
$n_{e0} = 22\,n_c$, $n_c = 1.8 \times 10^{21}\,\text{cm}^{-3}$
$t = 9.3$ Zyklen

3D, relativistic particle-in-cell simulations

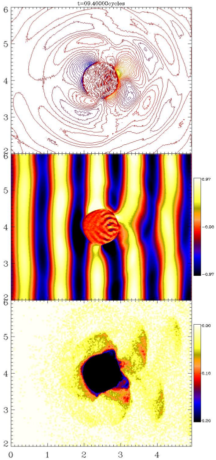

Felder $\mathbf{E} \parallel \mathbf{k}$, $\mathbf{E} \parallel \mathbf{E}_{\text{inc}}$ und Dichte

He-droplet, $R = 0.5\,\lambda$
$\lambda = 800\,\text{nm}$, 16 Zyklen $\sin^2$
$a = 1.0$ ($I \simeq 2 \times 10^{18}\,\text{Wcm}^{-2}$)
$n_{e0} = 22\,n_c$, $n_c = 1.8 \times 10^{21}\,\text{cm}^{-3}$
$t = 9.4$ Zyklen

3D, relativistic particle-in-cell simulations

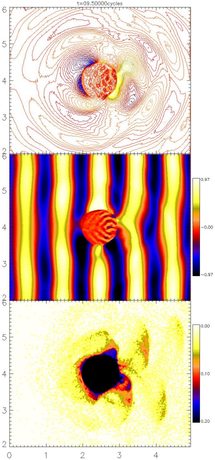

Felder $\mathbf{E} \parallel \mathbf{k}$, $\mathbf{E} \parallel \mathbf{E}_{\mathrm{inc}}$ und Dichte

He-droplet, $R = 0.5\,\lambda$
$\lambda = 800\,\mathrm{nm}$, 16 Zyklen $\sin^2$
$a = 1.0$ ($I \simeq 2 \times 10^{18}\,\mathrm{Wcm}^{-2}$)
$n_{e0} = 22\,n_c$, $n_c = 1.8 \times 10^{21}\,\mathrm{cm}^{-3}$
$t = 9.5$ Zyklen

3D, relativistic particle-in-cell simulations

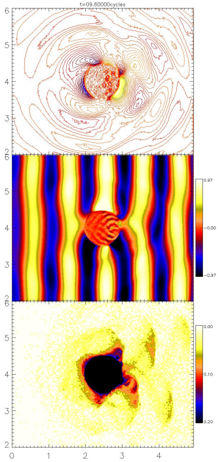

Felder $\mathbf{E} \parallel \mathbf{k}$, $\mathbf{E} \parallel \mathbf{E}_{\mathrm{inc}}$ und Dichte

He-droplet, $R = 0.5\,\lambda$
$\lambda = 800\,\mathrm{nm}$, 16 Zyklen $\sin^2$
$a = 1.0$ ($I \simeq 2 \times 10^{18}\,\mathrm{Wcm}^{-2}$)
$n_{e0} = 22\,n_c$, $n_c = 1.8 \times 10^{21}\,\mathrm{cm}^{-3}$
$t = 9.6$ Zyklen

3D, relativistic particle-in-cell simulations

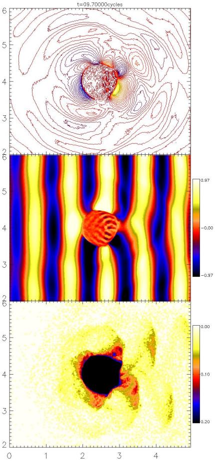

Felder $\mathbf{E} \parallel \mathbf{k}$, $\mathbf{E} \parallel \mathbf{E}_{\text{inc}}$ und Dichte

He-droplet, $R = 0.5\,\lambda$
$\lambda = 800\,\text{nm}$, 16 Zyklen $\sin^2$
$a = 1.0$ ($I \simeq 2 \times 10^{18}\,\text{Wcm}^{-2}$)
$n_{e0} = 22\,n_c$, $n_c = 1.8 \times 10^{21}\,\text{cm}^{-3}$
$t = 9.7$ Zyklen

3D, relativistic particle-in-cell simulations

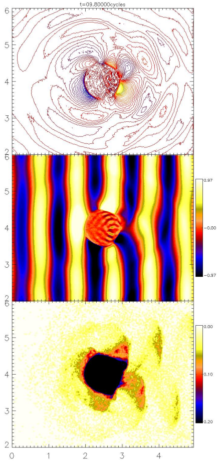

Felder $\mathbf{E} \parallel \mathbf{k}$, $\mathbf{E} \parallel \mathbf{E}_{\mathrm{inc}}$ und Dichte

He-droplet, $R = 0.5\,\lambda$
$\lambda = 800\,\mathrm{nm}$, 16 Zyklen $\sin^2$
$a = 1.0$ ($I \simeq 2 \times 10^{18}\,\mathrm{Wcm}^{-2}$)
$n_{e0} = 22\,n_c$, $n_c = 1.8 \times 10^{21}\,\mathrm{cm}^{-3}$
$t = 9.8$ Zyklen

3D, relativistic particle-in-cell simulations

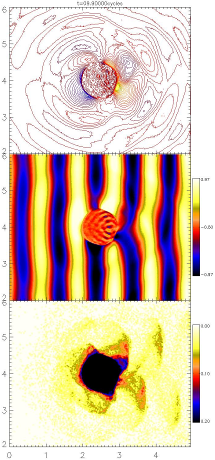

Felder $\mathbf{E} \parallel \mathbf{k}$, $\mathbf{E} \parallel \mathbf{E}_{\mathrm{inc}}$ und Dichte

He-droplet, $R = 0.5\,\lambda$
$\lambda = 800\,\mathrm{nm}$, 16 Zyklen $\sin^2$
$a = 1.0$ ($I \simeq 2 \times 10^{18}\,\mathrm{Wcm}^{-2}$)
$n_{e0} = 22\,n_c$, $n_c = 1.8 \times 10^{21}\,\mathrm{cm}^{-3}$
$t = 9.9$ Zyklen

3D, relativistic particle-in-cell simulations

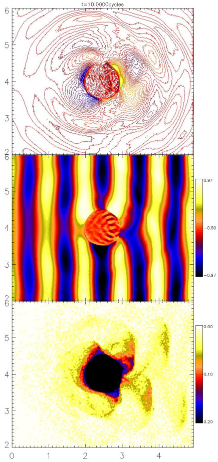

Felder **E** $\parallel$ **k**, **E** $\parallel$ $\mathbf{E}_{\text{inc}}$ und Dichte

He-droplet, $R = 0.5\,\lambda$
$\lambda = 800\,\text{nm}$, 16 Zyklen $\sin^2$
$a = 1.0$ ($I \simeq 2 \times 10^{18}\,\text{Wcm}^{-2}$)
$n_{e0} = 22\,n_c$, $n_c = 1.8 \times 10^{21}\,\text{cm}^{-3}$
$t = 10.0$ Zyklen